Title

Multi-degree-of-freedom ultrasonic micromotor for guidewire and catheter navigation: The NeuroGlide actuator

Journal

Applied Physics Letters, 100(16)

ISSN

0003-6951

Authors

Yun, Cheol-Ho
Yeo, Leslie Y
Friend, James R
et al.

Publication Date

2012-04-16

DOI

10.1063/1.3702579

Peer reviewed

AIP | Applied Physics Letters

Multi-degree-of-freedom ultrasonic micromotor for guidewire and catheter navigation: The NeuroGlide actuator

Cheol-Ho Yun, Leslie Y. Yeo, James R. Friend, and Bernard Yan

Citation: Appl. Phys. Lett. **100**, 164101 (2012); doi: 10.1063/1.3702579
View online: http://dx.doi.org/10.1063/1.3702579
View Table of Contents: http://apl.aip.org/resource/1/APPLAB/v100/i16
Published by the American Institute of Physics.

Multi-degree-of-freedom ultrasonic micromotor for guidewire and catheter navigation: The NeuroGlide actuator

Cheol-Ho Yun,[1] Leslie Y. Yeo,[1] James R. Friend,[1,a)] and Bernard Yan[2]
[1]*Micro/Nanophysics Research Laboratory, The Melbourne Centre for Nanofabrication, Clayton, Victoria 3800, Australia*
[2]*Neurointervention Unit, The Royal Melbourne Hospital, Parkville, Victoria 3052, Australia*

(Received 17 December 2011; accepted 20 January 2012; published online 16 April 2012)

A 240-μm diameter ultrasonic micromotor is presented as a potential solution for an especially difficult task in minimally invasive neurosurgery, navigating a guidewire to an injury in the neurovasculature as the first step of surgery. The peak no-load angular velocity and maximum torque were 600 rad/s and 1.6 nN-m, respectively, and we obtained rotation about all three axes. By using a burst drive scheme, open-loop position and speed control were achieved. The construction method and control scheme proposed in this study remove most of the current limitations in minimally invasive, catheter-based actuation, enabling minimally invasive vascular surgery concepts to be pursued for a broad variety of applications. © *2012 American Institute of Physics*. [http://dx.doi.org/10.1063/1.3702579]

Cerebrovascular disease is the leading cause of long term disability worldwide and a leading cause of death.[1] Minimally invasive vascular surgery (MIVS; Ref. 2) passes a long guidewire through the blood vessel system under x-ray visualization to reach the site of pathology. An endovascular catheter, complete with tools specific to the task, is subsequently guided along the guidewire to the location to treat, for example, strokes, aneurysms, and arterio-venous malformations.[3] The MIVS is often not possible due to the absence of dexterity of the surgeon's tools, the tortuosity of the neurovasculature,[4] and the limited time window within which the surgeon must reach the target location.[5]

To overcome these limitations, we propose an ultrasonic multi-degree of freedom (MDOF) micromotor, the NeuroGlide® actuator for steering the guidewire during navigation. Other approaches have been tried, including magnetic,[6] pull-wire,[7] hydraulic,[8] shape memory alloy,[9] and ionic polymer-metal composite[10] actuators, but they have drawbacks: either requiring a very long time to actuate, which are too large to navigate ~500 μm to 3 mm diameter arteries of the brain distal to the Circle of Willis, and are prone to failure, or offer only poor control.[11] Our aim is to offer a tip that can rotate at least 1 rad/s to offer visible (via x-ray) control to the surgeon and provide 1 nN-m torque about an axis perpendicular to the guidewire to accommodate turning forces as the guidewire is pushed along its route. We arrive at this figure by noting the rotating tip will be about 1 mm long, giving 1 μN of force at the tip upon contact with an artery wall, about what is needed for realistic, 5° deflections of the guidewire tip[12] to properly navigate. Though we aim to have a high-performance motor, a motor that is too powerful is actually dangerous as it can perforate the arterial wall and lead to potentially fatal brain hemorrhage. Piezoelectric ultrasonic microactuators and micromotors[13–15] are attractive for MIVS, offering simplicity, high torque-to-weight ratio, inherent braking, precise positioning accuracy, and flexibility in design.

Most MDOF ultrasonic motors generate rotation about an arbitrary axis by combining the vibrations of a set of orthogonal vibration modes, for example, two orthogonal bending vibration modes and a longitudinal vibration mode,[16–18] each of which are designed to generate rotation about a particular axis. However, in order to generate the three independent vibration modes, at least one ground and four signal input electrodes (and five lead wires each with a diameter of 50 μm) are required; work conducted in our laboratory under our direction by a former student[19] is emblematic of this problem: so many lead wires along the catheter present insurmountable problems in transmission loss, fabrication, and mutual induction losses. Further, controlling the vibration in this system with matched resonance frequencies is impossible due to degeneracy of the bending modes,[20] a phenomenon that has been known for a long time.[21] Worst of all, relying on so many vibration modes in *symmetric* designs is fraught with fabrication problems: Should there be any fabrication mistake or damage during use, the coupling and resonance frequencies can and do change, either causing the motor to stop working or become uncontrollable? At these scales, fabricating such motors for actual applications is simply unrealistic.

Here, we purposely introduce an "error:" a tilt in a component of the structure, making the 240 μm diameter motor far easier to construct and use, because construction flaws become tolerable rather than unsurmountable, and the motor can be operated with only three lead wires. The MDOF motor in Fig. 1 uses only two signal input electrodes attached to two electroded faces of the PZT (C–203 lead zirconate titanate, Fuji Ceramics, Ltd., Tokyo, Japan) along the x axis and a single electrode on the bottom of the PZT element on the z axis; the PZT element itself is polarized along the z-axis direction. Only three wires are necessary for connection. When a sinusoidal voltage potential is applied between one of the x-face electrodes and the ground electrode, both shear and longitudinal strains can be excited simultaneously, deforming the PZT element with transverse bending along the xz plane and axial strain along the z axis due to shear

a)Electronic mail: james.friend@rmit.edu.au.

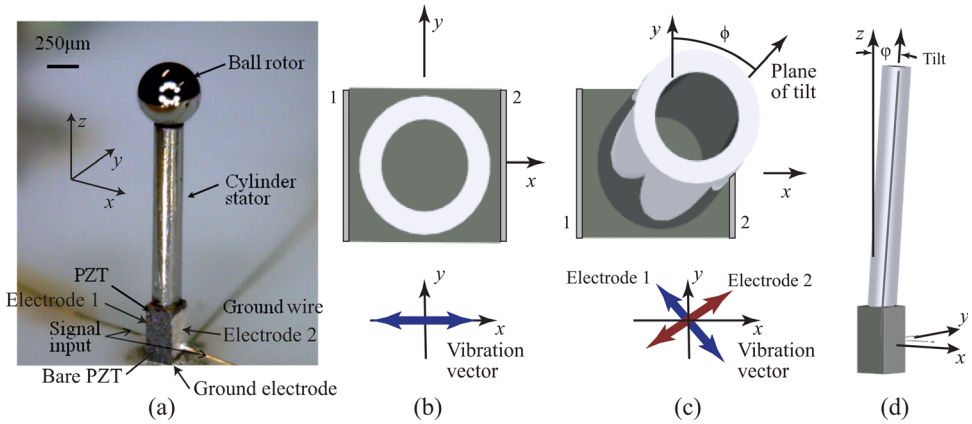

FIG. 1. (a) The motor is reminiscent of our previous simple single-axis motor,[13] but cuts in the tubing are unnecessary here because of the noticeable tilt producing modal coupling. Looking at the stator from the top, without (b) tilt of the tube, the structure is symmetric, and inducing vibration with electrodes 1 and 2 as shown can only generate vibration in the xz plane. If the tube is (c) and (d) tilted by φ in a plane, it is rotated about z by an angle of $\phi \neq 0$ from the positive y-axis, bending vibration about an arbitrary axis may be obtained with only the side electrodes (1,2; also shown in (a)). Taking (d) the page as the plane of tilt, a different view of the amount of tilts, φ, can be shown.

coupling through e_{15} inverse piezoelectric effects.[22] The motion generated by the combined bending and axial deformation of the PZT element causes, likewise, bending and axial deformation in a simple cylinder mounted atop it.

Bending and axial vibration with a temporal phase difference can be simultaneously excited by applying two signals to the side electrodes possessing a temporal phase difference. Because the coupling is via the tilted tube, the input phase difference is not the same as the output phase difference, but the latter may be controlled to obtain elliptical motion at the tip of the stator that, in turn, can be used to rotate an object placed upon the tip. If the tubing of the stator is aligned symmetrically along the z axis (Fig. 1(b)), such elliptical motion of the stator tip can only be generated in the z–x plane, because the stator's bending along the y–z plane is uncoupled from the motion that can be generated with the chosen electrode configuration. However, introducing an asymmetry—the tube's *tilt*—into the structure, it is possible to couple the bending along the y–z plane into the motion generated along the x–z plane, making it possible to drive y–z plane bending vibration through the electrodes on the x-axis faces.[23,24] When the metal cylinder tube is mounted on the PZT with a tilt of ϕ along a direction slightly away from the y-axis and toward the x-axis, as defined by the angle φ, all as shown in Fig. 1(c), the stator's vibrations in the yz-plane are then coupled with vibrations in the xz-plane. Vibration of the stator in the yz-plane can then be generated through excitation of bending vibration in the xz-plane. In this configuration, the vibration vector of the stator tip due to the excitation of "electrode 1" on the positive x-axis face of the PZT element (see Fig. 1(a)) has an orientation along a different plane than when exciting "electrode 2" on the negative x-axis face of the PZT element. By changing the phase between the two electrodes, the orientation of the tip motion can be changed. Using this arrangement, we can control the elliptical vibration direction of the cylinder tip about an arbitrary axis, resulting in arbitrary motion of a rotor placed in contact with this tip.

Modal and harmonic analysis of the stainless steel (304; 240 μm outer and 110 μm inner diameter) stator including a PZT element $250 \times 250 \times 500\,\mu\text{m}^3$ in size, an epoxy bond (7 μm thick) between the PZT and the tube, and Ag/Cr electrodes (15 μm thick) was performed using ANSYS (ANSYS Inc., Canonsburg, PA, USA) to predict the tilted coupling effect. The PZT element size was fixed at $250 \times 250 \times 500\,\mu\text{m}^3$ due to fabrication limitations and the practical need to define the motor's scale for its intended application. The tube was mounted with a tilt of $\varphi = 10^\circ$ in a plane placed at an angle of $\phi = 2^\circ$ from the y-axis and toward the x-axis (see Fig. 1); these angles were selected after exploratory analysis to determine a suitable arrangement that could be reliably fabricated. Though the tilt and the dimensions were constrained due to fabrication limitations, fortunately the simple adjustment of the length was sufficient to permit resonance frequency matching of the first longitudinal, third xz-plane bending, and third yz-plane bending modes at a cylinder length of 1.6 mm as shown in Fig. 2.

Since the cylinder is tilted toward the y-axis and the electrode layer is only present on the x-axis faces of the PZT, the bending stiffnesses of the stator along the xz and yz

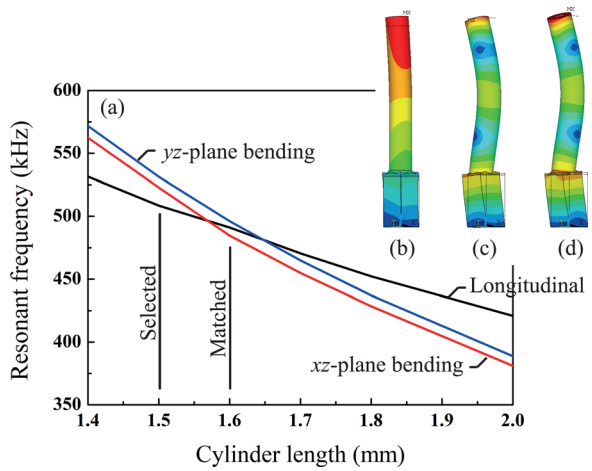

FIG. 2. Changing (a) the cylinder length permits matching of resonance frequencies of the flexural and axial vibrations in the structure at about 1.6 mm. While this is appropriate for a naïve design; choosing this length would result in uncontrollability due to degenerate modes, and so we choose a slightly shorter length of 1.5 mm for the structure to give the (b) first longitudinal, (c) y-axis third bending, and (d) x-axis third bending modes according to analysis.

planes are different. Likewise, the resonance frequencies of the bending modes along these two planes are also expected to be different—the reason for the difference seen in Fig. 2(a), and so precise matching of resonance frequencies is not possible. This is actually desirable, however, and indeed, we chose a cylinder length of 1.5 mm to *increase* the mismatch in resonance frequencies; the mode shapes are illustrated in Figs. 2(c)–2(e). A closely matched resonance system easily causes uncontrollable coupled vibration due to frequency degeneracy as described previously. Each of the modes is not a pure mode of vibration; the longitudinal mode shows some bending as a consequence of the coupling through the tilted stainless steel cylinder. Likewise, each bending mode show longitudinal motion and deflection along planes not parallel to either the x or y axes. Since the tip motions, in particular, are orthogonal and collectively span the entire vector space, rotation of a rotor placed upon the tip about an arbitrary axis is possible with a suitable combination of these vibration modes.

The harmonic response of the stator was calculated from 450 to 550 kHz, spanning the design range for the 1.5 mm tube. The only three resonance peaks to appear were present at 508.5, 522.8, and 531.4 kHz, corresponding to the longitudinal, yz-plane bending, and xz-plane bending vibration mode frequencies, respectively.

The tube was cut by laser machining and mounted on the PZT top using nonconductive epoxy in a painstaking process developed by Watson;[13,25] a completed motor is shown in Fig. 1(a). Drive signals were supplied to the transducer via 50-μm diameter Au wires attached to the PZT electrodes using conductive epoxy (Epotek H20E, Elecsys LLC, USA). A stainless steel ball (ϕ, 0.5 mm), atop the tube in contact along its inner diameter, was retained with a magnetic preload through the presence of a permanent magnet on the bottom of the PZT element. Rotation is generated through stick-slip contact from the elliptical vibration of the stator such that the rotation axis of the ball is generally perpendicular to the plane of the vibration of the stator tip.

The vibration modes and frequency spectrum of the stator tip were measured using a scanning laser Doppler vibrometer (LDV) (Polytec MSA–400, Waldbrunn, Germany) as shown in supplementary material.[30] The yz and xz-plane bending resonances appear in our prototype at 520 kHz and 531 kHz, corresponding to the analytical predictions of 522.8 kHz and 531.4 kHz, respectively. By driving the x-axis electrodes near the yz-plane bending resonance frequency, the yz-plane bending motion can be generated.

Figure 3 shows the measured transient response of the ball rotor velocity along three orthogonal axes with respect to time using a laser Doppler tachometer (Canon LVZ, Tokyo Japan), with a dynamic first-order lag response[26] fitting fairly well, except for an obvious rotor bounce[27] causing oscillation in the response, especially during z-axis rotation. Using Nakamura's method[26] to determine the speed-torque characteristics of the motor for a measured preload of 0.76 mN, the torque is shown over the range of rotation speeds for our system in Fig. 3(b), all at an applied voltage of 15 V_{RMS}.

For many MDOF ultrasonic motors, the direction of rotation is reversed by simply changing the driving phase between the input electrodes. However, not only the direction but also the *axis* of rotation changes when the phase angle between the two electrodes is changed. One has to therefore exercise a bit more care in controlling the motion. At a driving frequency of 518 kHz and a phase difference between the two input electrodes of 20°, the ball rotor rotates along the x-axis. However, the ball rotor spins only in the counter clockwise (CCW) direction. By changing the driving phase, the ball rotor changes its rotation axis direction but rotation in the clockwise (CW) direction along the x-axis was not obtained—the reason for this is not entirely clear, as the vibration behavior indicates CW rotation about the x-axis should be possible. When the phase between the two signal inputs is fixed at 90°, the ball rotor rotates along an arbitrary rotation axis as defined by the driving frequency. However, CCW and CW rotations about the y-axis were obtained at 521 kHz and 531 kHz, respectively. For z-axis rotation, the operating frequencies for CCW and CW directions were 520 kHz and 530 kHz, respectively, all while using a phase difference of 10°. Consequently, rotation about each of the three orthogonal axes x, y, and z can be obtained using specific driving combinations of frequency and phase difference. The maximum torque and rotation speed along the x, y, and z axes were 1.3 nN-m and 400 rad/s, 1.6 nN-m and 600 rad/s, and 0.65 nN-m and 550 rad/s, respectively.

Open-loop control using short-time, high-power sinusoidal *burst drive* signals[20,28] provides a compact method for operating the motor without an impossibly large position

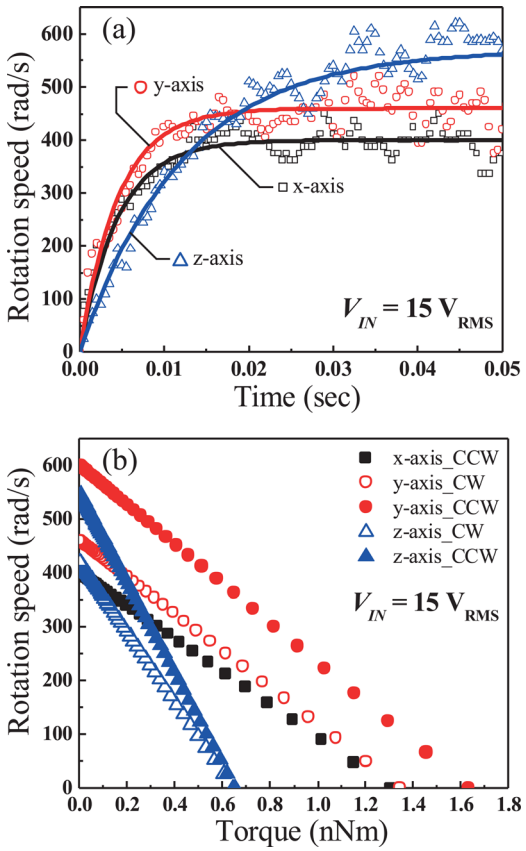

FIG. 3. The (a) transient response of the motor along three orthogonal axes over time, indicating the motor can be operated about all three axes at speeds of at least 350 rad/s with only 15 V_{RMS}. (b) Torque-speed characteristics of the motor at a preload of 0.76 mN and 15 V_{RMS} as determined using Nakamura's method (see Ref. 26).

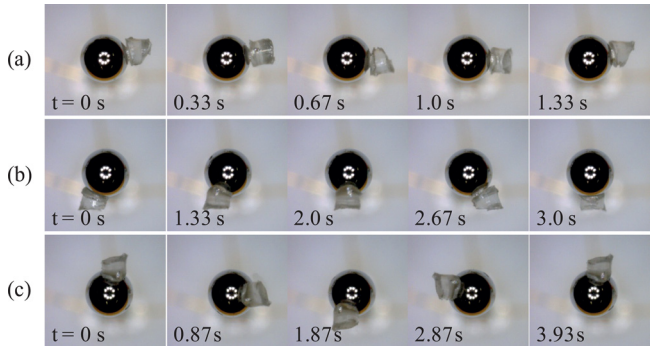

FIG. 4. The operation of the motor at 15 V_{RMS} using an open-loop burst drive scheme: controlled rotation about the (a) *x*-axis, (b) *y*-axis, and (c) *z*-axis. The *x*-axis rotation is shown with 700 wavelengths signal on, followed by 100 000 wavelengths off; the other two rotations are shown with 450 and 100 000 wavelengths on and off, respectively. Each image shows the rotor between input bursts (enhanced online) [URL: http://dx.doi.org/10.1063/1.3702579.1].

sensor placed on the rotor. The rotor displacement is roughly linear with respect to the burst duration of the input signal when the burst duration is shorter than the rise time of the rotor velocity.[29] The operation of the motor using the controlled burst drive scheme is illustrated in Fig. 4.

The ball rotor was operated as a stepping motor about the *x*, *y*, and *z* axes; rotation about an arbitrary axis can be obtained by combining these rotations together in a linear fashion. CCW and CW rotations were possible for the *y* and *z* axes, while CW rotation was possible for the *x* axis; since the rotation speed exceeds 350 rad/s about any axis, the orientation of the rotor can be changed to point at any direction in less than 30 ms even with this limitation, even with the presence of an object on the rotor that prevents its complete rotation as with the small attachment shown on the rotor in Fig. 4. In addition, the rotation speed may be changed by adjusting the burst duration and interpulse interval. In Fig. 4(a), the *x*-axis rotation is much faster than the others, because the burst duration was set to 700 wavelengths. Rotation about an arbitrary axis can be easily obtained by combining discrete combinations of burst signals at the defined frequencies and phases. Expansion of these combinations to other axes and rotation directions is currently under study. Control through the burst drive scheme, though not precise, is likely to be ideal for applications with space limitations sufficient to demand such small motors in the first place, including MIVS.

The authors wish to acknowledge the support of this work by funding provided to them by the NHMRC through Development Grant No. 546238 and the CASS Foundation through Grant No. SM/07/1616.

[1]V. Feigin, C. Lawes, D. Bennett, S. Barker-Collo, and V. Parag, Lancet Neurol. **8**, 355 (2009).
[2]S. Renowden, J. Neurol., Neurosurg. Psychiatry **76**, iii48 (2005).
[3]E. Laws, J. Neuroophthalmol. **28**, 366 (2008).
[4]M. Söderman, D. Babic, R. Homan, and T. Andersson, Neuroradiol. **47**, 735 (2005).
[5]R. Chewning, G. Wyse, and K. Murphy, Semin. Intervent. Radiol. **25**, 42 (2008).
[6]S. Ramcharitar, M. Patterson, R. van Geuns, C. van Meighem, and P. Serruys, Nat. Clin. Pract. Cardiovasc. Med. **5**, 148 (2008).
[7]P. Kanagaratnam, M. Koa-Wing, D. Wallace, A. Goldenberg, N. Peters, and D. Davies, J. Interv. Card. Electrophysiol. **21**, 19 (2008).
[8]K. Ikuta, H. Ichikawa, K. Suzuki, and D. Yajima, in *Proceedings of the 2006 IEEE International Conference on Robotics and Automation, ICRA 2006* (IEEE, 2006), pp. 4161–4166.
[9]K. Park and M. Esashi, J. Microelectromech. Syst. **8**, 349 (2002).
[10]B. Fang, M. Ju, and C. Lin, Sens. Actuators, A **137**, 321 (2007).
[11]Y. Fu, H. Liu, W. Huang, S. Wang, and Z. Liang, Int. J. Med. Robotics Computer Assisted Surg. **5**, 381 (2009).
[12]C. Putman, J. Chaloupka, P. Kailasnath, and J. Alderman, Invest. Radiol. **32**, 241 (1997).
[13]B. Watson, J. Friend, and L. Yeo, J. Micromech. Microeng. **20**, 115018 (2010).
[14]B. Watson, L. Yeo, and J. Friend, Rev. Sci. Instrum. **81**, 063901 (2010).
[15]B. Watson, J. Friend, and L. Yeo, Sens. Actuators, A **152**, 219 (2009).
[16]T. F. Khoo, D. Dang, J. Friend, D. Oetomo, and L. Yeo, IEEE Trans. Ultrason. Ferroelectr. Freq. Control **56**, 1716 (2009).
[17]Y. Gouda, K. Nakamura, and S. Ueha, Ultrasonics **44**, e617 (2006).
[18]H. Kawano, H. Ando, T. Hirahara, C. Yun, and S. Ueha, IEEE Trans. Robotics **21**, 790 (2005).
[19]G. Rogers, J. Micromech. Microeng. **20**, 125002 (2010).
[20]Y. Cheol-Ho, S. Niwano, J. Friend, K. Nakamura, and U. Sadayuki, Jpn. J. Appl. Phys. Part I **42**, 3000 (2003).
[21]S. Hansen and E. Zuazua, SIAM J. Control Optim. **33**, 1357 (1995).
[22]J. Friend and L. Yeo, "Encyclopedia of micro- and nanofluidics," in *Piezoelectric Materials for Microfluidics* (Springer, New York, NY, USA, 2008), pp. 1654–1662.
[23]M. Kurosawa and S. Ueha, J. Acoust. Soc. Am. **90**, 1723 (1991).
[24]M. Aoyagi and Y. Tomikawa, Jpn. J. Appl. Phys. Part I **32**, 4190 (1993).
[25]B. Watson, J. Friend, and L. Yeo, J. Micromech. Microeng. **19**, 022001 (2009).
[26]K. Nakamura, M. Kurosawa, H. Kurebayashi, and S. Ueha, IEEE Trans. Ultrason. Ferroelectr. Freq. Control **38**, 481 (2002).
[27]K.-C. Liu, J. Friend, and L. Yeo, Phys. Rev. E **80**, 046201 (2009).
[28]S. Niwano, C. Yun, J. Friend, K. Nakamura, and T. Ueha, IEICE Technical Report US2003-92 (Institute of Electronics, Information and Communication Engineers, 2003), Vol. 103, p. 43.
[29]W. Kim, C. Yun, and S. Lee, Jpn. J. Appl. Phys. **47**, 5687 (2008).
[30]See supplementary material at http://dx.doi.org/10.1063/1.3702579 for information on laser Doppler vibrometry used to determine the vibration shapes of the stator in this motor prototype as it undergoes different driving configurations.

AIP | Applied Physics Letters

50th ANNIVERSARY EDITOR'S PICKS

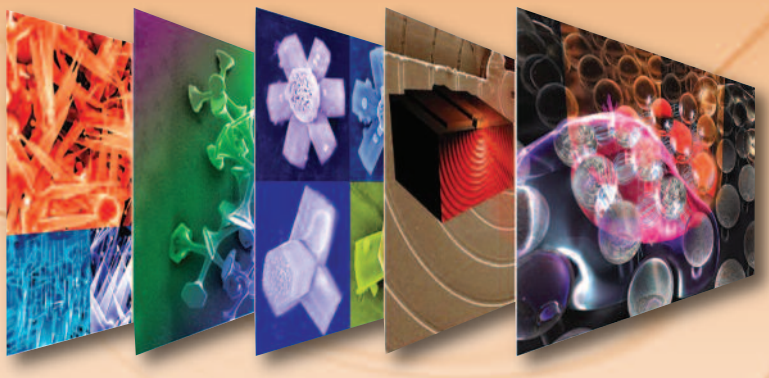

AIP | Publishing

apl.aip.org/50th_anniversary_editors_picks

Editors

APL 50TH ANNIVERSARY EDITOR'S PICKS

In this collection, the Editor has selected a few of the many notable APL articles published from 2009 through 2012 that present ground-breaking research. This collection illustrates only a small fraction of the critical research published in APL over the past fifty years but is representative of the broad cross section of topics that the Journal covers. The articles listed in the collection are freely available online at apl.aip.org until the end of September 2013.

Celebrating 50 Years of *Applied Physics Letters*!

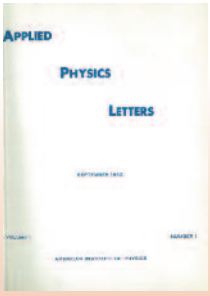

First cover in 1962

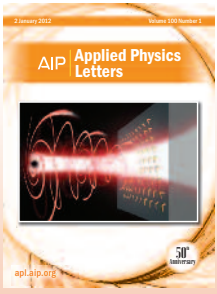

2012 cover

Collection of Cover Images (2003–2011)

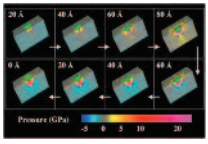

Vol 82 Issue 1

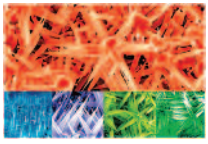

Vol 84 Issue 15

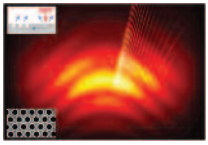

Vol 87 Issue 10

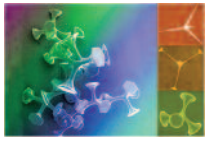

Vol 88 Issue 19

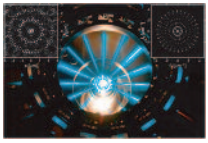

Vol 88 Issue 26

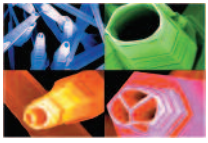

Vol 90 Issue 11

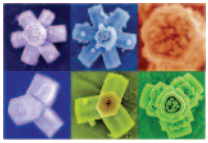

Vol 90 Issue 12

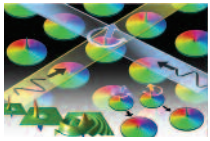

Vol 92 Issue 2

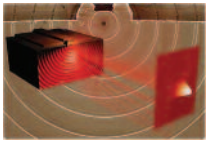

Vol 93 Issue 18

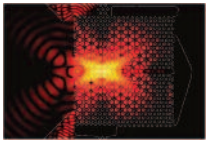

Vol 94 Issue 11

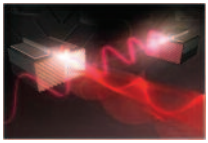

Vol 94 Issue 15

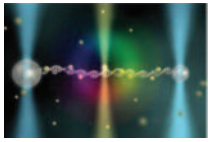

Vol 96 Issue 21

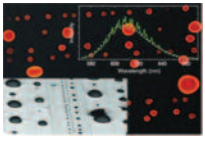

Vol 97 Issue 21

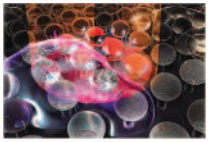

Vol 98 Issue 15

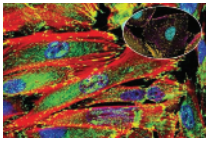

Vol 99 Issue 6

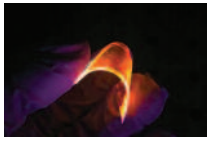

Vol 99 Issue 24

The #1 Journal in Citations in Applied Physics Category*

Applied Physics Letters, published by the American Institute of Physics, features concise, up-to-date reports on significant new findings in applied physics. Emphasizing rapid dissemination of key data and new physical insights, *Applied Physics Letters* offers prompt publication of new experimental and theoretical papers bearing on applications of physics phenomena to all branches of science, engineering, and modern technology.

**2011 Journal Citation Reports®* (Thomson Reuters, 2012)

EDITORS

1962 . . . . . James H. Crawford, Jr.
1964 . . . . . Frank E. Myers
1970 . . . . . Foster F. Rieke
1970 . . . . . Gilbert J. Perlow
1975 . . . . . Thomas H. Braid, Acting Editor
1975 . . . . . Gilbert J. Perlow
1990 . . . . . Hartmut Wiedersich
1994 . . . . . Nghi Q. Lam

WHY PUBLISH WITH APL?

Highly Cited

Ranked #1 in citations in the Applied Physics category, with 203,336 total citations in 2011*

**2011 Journal Citation Reports*® (Thomson Reuters, 2012)*

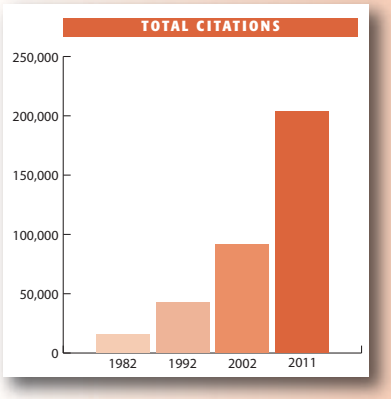

Impact Factor

3.844*

**2011 Journal Citation Reports*® (Thomson Reuters, 2012)*

Must-Have

Applied Physics Letters* consistently ranks in the top 25 of the world's 50,000 most-used journals*

***bX Journal Popularity Report* (ExLibris, Q1 2012).

Premier Quality

APL's editorial team comprises 34 prestigious international researchers who oversee the entire peer-review process. Their goal is to select only the best, most significant and most timely work for publication in the Journal.

Well-Read

APL boasts more than five million article downloads in 2011, reflecting broad appeal to a diverse scientific community.

Rapid Publication

The median processing time from submission to acceptance is less than 60 days, publishing your important results faster.

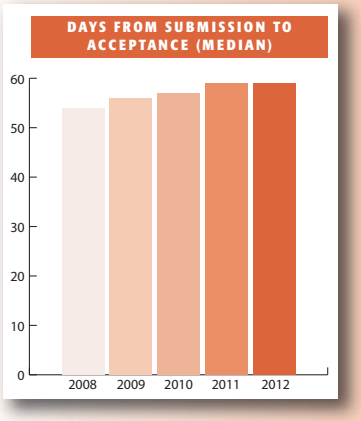

Submit your research findings at apl.peerx-press.org to experience a wide range of valuable benefits

High Visibility for Your Work

1. *Research Highlights* — Freely available articles spotlighting some of today's most interesting research
2. *Top 20 Most Read* — A collection of APL's most popular papers each month
3. *Top 20 Most Cited* — A collection of APL's most highly-cited articles; the foundation of current research
4. *Top Stories* — Your APL articles are big news! We aggregate all the Press Releases for APL articles into one convenient location. See what's making headlines!
5. *Editor's Picks* — A cross section of articles the Editor recommended, representing the best of what APL has to offer.

"I truly appreciate all of your effort in resolving matters connected with the disposition of this manuscript, and for keeping me informed while the difficulties with electronic communication were resolved. The prompt, courteous, and expert assistance you have offered in this particular instance is one of the reasons that APL and JAP remain top choices for the publication of our work."

– George A. Rossetti, Jr.
Associate Professor of Materials Science & Engineering,
Institute of Materials Science,
University of Connecticut

The most up-to-date experimental and theoretical results impacting applications of physics to all branches of science and technology. Coverage includes a range of topics in the fields of:

- Photonics and Optoelectronics
- Surfaces and Interfaces
- Structural, Mechanical, Optical, and Thermodynamic Properties of Advanced Materials
- Semiconductors
- Magnetics and Spintronics
- Superconductivity and Superconducting Electronics
- Dielectrics, Ferroelectrics, and Multiferroics
- Nanoscale Science and Technology
- Organic Electronics and Photonics
- Device Physics
- Biophysics and Bio-inspired Systems
- Energy Conversion and Storage
- Interdisciplinary and General Physics

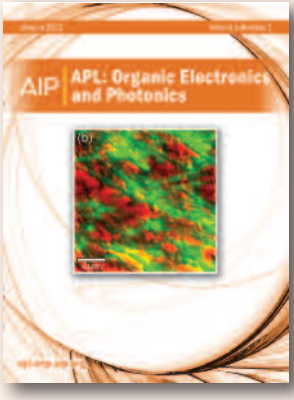

Did you know?
APL-OEP articles freely available online!

APL: Organic Electronics and Photonics (APL-OEP) is a compilation of the hottest research in organic electronics and photonics. The spotlight journal is a subset of *Applied Physics Letters*. Articles presented in APL-OEP are freely available to the research community at apl-oep.aip.org.

Voltage modulation of a vertical cavity transistor laser via intra-cavity photon-assisted tunneling

Mong-Kai Wu, Milton Feng, and Nick Holonyak, Jr.

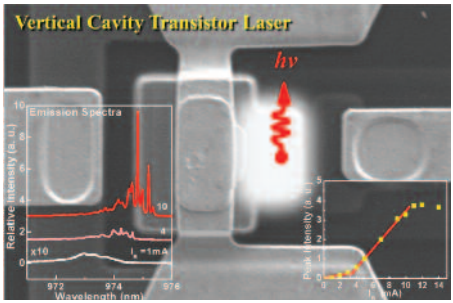

The authors report the direct voltage modulated operation of a vertical cavity transistor laser (VCTL) via intra-cavity coherent photon-assisted tunneling. The reversed-bias base/collector junction of the transistor laser provides high input impedance for effective high-speed direct voltage modulation. The optical L-V_{CE} characteristics show that the emission intensity saturates and then decreases in laser intensity to half amplitude and broadens when V_{CE} is switched from 3 to 6 V owing to intra-cavity photon-assisted tunneling at the base/collector junction. Correspondingly, the collector I_C-V_{CE} characteristics exhibit increased current at higher V_{CE}.

Appl. Phys. Lett. **101**, 081102 (2012)

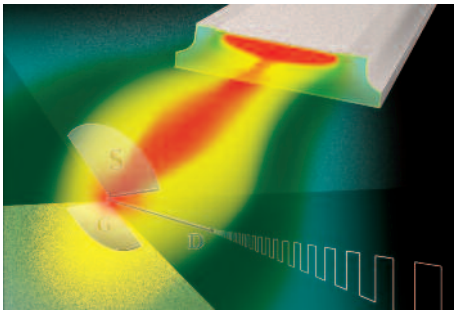

Semiconductor nanowires for highly sensitive, room-temperature detection of terahertz quantum cascade laser emission

Miriam S. Vitiello, Leonardo Viti, Lorenzo Romeo, Daniele Ercolani, G. Scalari, J. Faist, F. Beltram, L. Sorba, and A. Tredicucci

The authors report the development of nanowire-based field-effect transistors operating as high sensitivity terahertz (THz) detectors. By feeding the 1.5 THz radiation field of a quantum cascade laser (QCL) at the gate-source electrodes with a wide band dipole antenna, they record a photovoltage signal corresponding to responsivity values >10 V/W, with impressive noise equivalent power levels $<6\times10^{-11}$ W/$\sqrt{\text{Hz}}$ at room temperature and a wide modulation bandwidth. The potential scalability to even higher frequencies and the technological feasibility of realizing multi-pixel arrays coupled with QCL sources make the proposed technology highly competitive for a future generation of THz detection systems.

Appl. Phys. Lett. **100**, 241101 (2012)

Flexible distributed-feedback colloidal quantum dot laser

Yujie Chen, Benoit Guilhabert, Johannes Herrnsdorf, Yanfeng Zhang, Allan R. Mackintosh, Richard A. Pethrick, Erdan Gu, Nicolas Laurand, and Martin D. Dawson

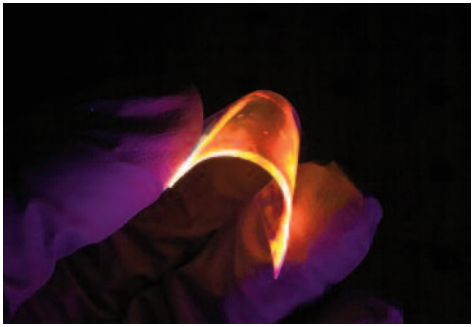

By fabricating a submicron-scale grating structure on a bendable polymer substrate, the authors demonstrate a flexible distributed-feedback colloidal quantum dot laser. This laser uses cadmium selenide/zinc sulfide core-shell nanostructures, operating in transverse electric polarized multiple-modes, and has a typical threshold pump fluence of ~4 mJ/cm^2.

Appl. Phys. Lett. **99**, 241103 (2011)

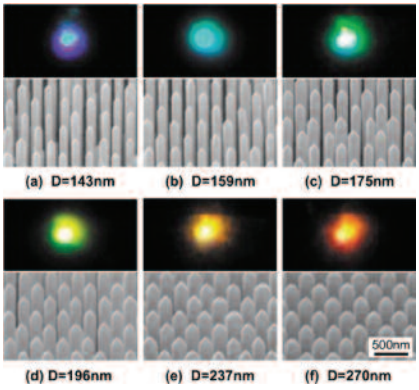

Emission color control from blue to red with nanocolumn diameter of InGaN/GaN nanocolumn arrays grown on same substrate

Hiroto Sekiguchi, Katsumi Kishino, and Akihiko Kikuchi

A novel technology for controlling the In composition of InGaN quantum wells on the same wafer was developed, which paved the way for the monolithic integration of three-primary-color nano-light-emitting diodes. In the experiment, InGaN/GaN multiple quantum well nanocolumn arrays with nanocolumn diameters from 137 to 270 nm were prepared on the same substrate with the Ti-mask selective area growth by rf-plasma-assisted molecular beam epitaxy. The emission color changed from blue to red (from 479 to 632 nm in wavelength) with increasing nanocolumn diameter. The emission color change mechanism was clearly explained by the beam shadow effect of the neighboring nanocolumns.

Appl. Phys. Lett. **96**, 231104 (2010)

Multi-beam multi-wavelength semiconductor lasers

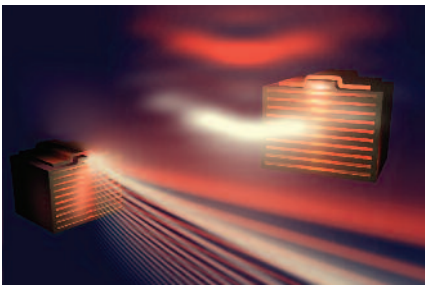

Nanfang Yu, Mikhail A. Kats, Christian Pflügl, Markus Geiser, Qi Jie Wang, Mikhail A. Belkin, Federico Capasso, Milan Fischer, Andreas Wittmann, Jérôme Faist, Tadataka Edamura, Shinichi Furuta, Masamichi Yamanishi, and Hirofumi Kan

Multibeam emission and spatial wavelength demultiplexing in semiconductor lasers by patterning their facets with plasmonic structures is reported. Specifically, a single-wavelength laser was made to emit beams in two directions by defining on its facet two metallic gratings with different periods. The output of a dual-color laser was spatially separated according to wavelength by using a single metallic grating. The designs can be integrated with a broad range of active or passive optical components for applications such as interferometry and demultiplexing.

Appl. Phys. Lett. **95**, 161108 (2009)

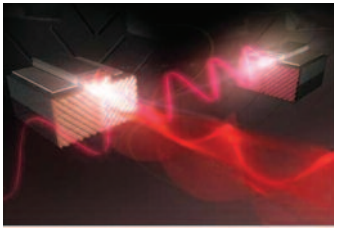

Semiconductor lasers with integrated plasmonic polarizers

Nanfang Yu, Qi Jie Wang, Christian Pflügl, Laurent Diehl, Federico Capasso, Tadataka Edamura, Shinichi Furuta, Masamichi Yamanishi, and Hirofumi Kan

The authors reported the plasmonic control of semiconductor laser polarization by means of metallic gratings and subwavelength apertures patterned on the laser emission facet. An integrated plasmonic polarizer can project the polarization of a semiconductor laser onto other directions. By designing a facet with two orthogonal grating-aperture structures, a polarization state consisting of a superposition of a linearly and right-circularly polarized light was demonstrated in a quantum cascade laser; a first step toward a circularly polarized laser.

Appl. Phys. Lett. **94**, 151101 (2009)

High-speed switching of spin polarization for proposed spin-photon memory

V. Zayets and K. Ando

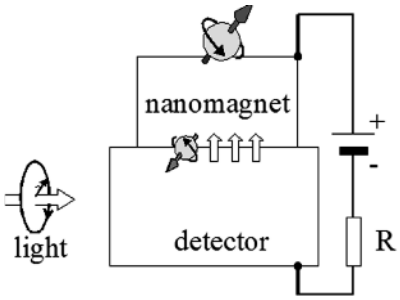

Nonvolatile high-speed optical memory is proposed, which utilizes the magnetization reversal of nanomagnet by spin-polarized photoexcited electrons. It was demonstrated experimentally that one selected pulse from the train of two optical data pulses with interval of 450 fs can solely excite the spin-polarized electrons without a disturbance from the unselected optical data pulse. That proves feasibility for operation of the memory with speed of 2.2 Tbits/s.

Appl. Phys. Lett **94**, 121104 (2009)

STRUCTURAL, MECHANICAL, OPTICAL, & THERMODYNAMIC PROPERTIES OF ADVANCED MATERIALS

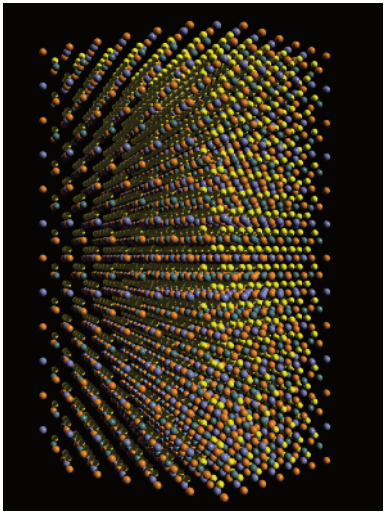

Bandgap engineering of $ZnSnP_2$ for high-efficiency solar cells

David O. Scanlon and Aron Walsh

$ZnSnP_2$, an absorber material for solar cells, transitions from an ordered chalcopyrite to a disordered sphalerite structure at high temperatures. The authors investigate the electronic structure of both phases, combining a screened hybrid density functional with the special quasi-random structure method. They predict a bandgap reduction of 0.95 eV between the ordered and fully disordered materials. Experimental reports are consistent with partial disorder. Tuning of the order parameter would lead to a family of $ZnSnP_2$ phases with bandgaps ranging from 0.75 eV to 1.70 eV, thus providing graded solar cell absorbers from a single material system.

Appl. Phys. Lett. **100**, 251911 (2012)

Photo-origami—Bending and folding polymers with light

Jennie Ryu, Matteo D'Amato, Xiaodong Cui, Kevin N. Long, H. Jerry Qi, and Martin L. Dunn

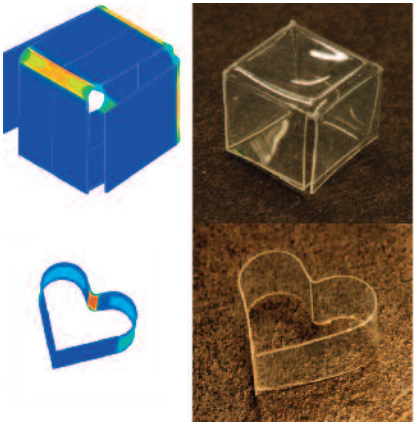

Photo-origami uses the dynamic control of the molecular architecture of a polymer by a combination of mechanical and non-contact optical stimuli to design and program spatially and temporally variable *mechanical and optical fields* into a material. The fields are essentially actuators, embedded in the material at molecular resolution, designed to enable controllable, sequenced, macroscopic bending and folding to create three-dimensional material structures. The authors demonstrate, through a combination of theory, simulation-based design, synthesis, and experiment, the operative phenomena and capabilities of photo-origami that highlight its potential as a powerful, and potentially manufacturable, approach to create three-dimensional material structures.

Appl. Phys. Lett. **100**, 161908 (2012)

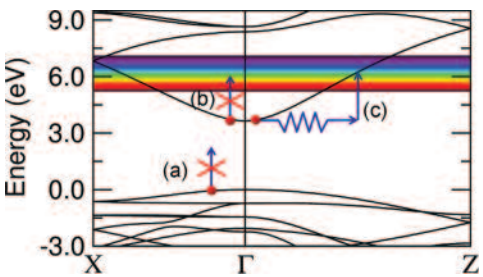

Fundamental limits on optical transparency of transparent conducting oxides: Free-carrier absorption in SnO_2

H. Peelaers, E. Kioupakis, and C. G. Van de Walle

Transparent conducting oxides combine high electrical conductivity with transparency to visible light. However, the large concentration of free electrons introduces a source of absorption that limits the transparency. The authors evaluate the importance of phonon-assisted free-carrier absorption in SnO_2 completely from first principles. Their results show that absorption is modest in the visible and much stronger in the UV and infrared. They also provide insight into the mechanisms that govern absorption in different wavelength regimes.

Appl. Phys. Lett. **100**, 011914 (2012)

Mechanics of hemispherical electronics

Shuodao Wang, Jianliang Xiao, Inhwa Jung, Jizhou Song, Heung Cho Ko, Mark P. Stoykovich, Yonggang Huang, Keh-Chih Hwang, and John A. Rogers

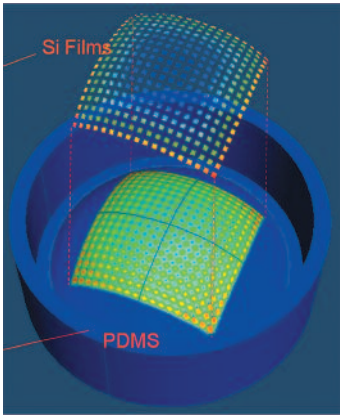

A simple analytical model is established for the development of hemisphere electronics, which has many important applications in electronic-eye cameras and related curvilinear systems. The photodetector arrays, made in planar mesh layouts with conventional techniques, are deformed and transferred onto a hemisphere. The model gives accurately the positions of photodetectors on the hemisphere, and has been validated by experiments and finite element analysis. The results also indicate very small residual strains in the photodetectors. The model provides a tool to define a pattern of photodetectors in the planar, as-fabricated layout to yield any desired spatial configuration on the hemisphere.

Appl. Phys. Lett. **95**, 181912 (2009)

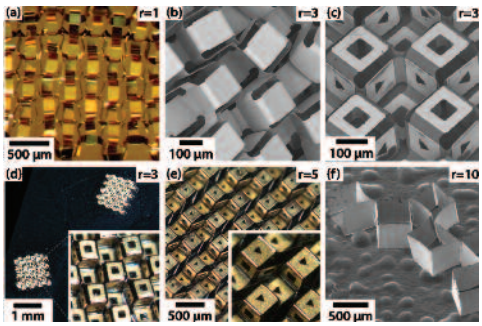

Microassembly based on hands free origami with bidirectional curvature

Noy Bassik, George M. Stern, and David H. Gracias

Microassembly based on origami, the Japanese art of paper folding, presents an attractive methodology for constructing complex three-dimensional (3D) devices and advanced materials. A variety of functional structures have been created using patterned metallic, semiconducting, and polymeric thin films, but have been limited to those that curve in a single direction. The authors report a design framework that can be used to achieve spontaneous bidirectional folds with any desired angle, and they demonstrate theoretical and experimental realizations of complex 3D structures with +90°, −90°, +180°, and −180° folds. The strategy is parallel, versatile, and compatible with conventional microfabrication.

Appl. Phys. Lett. **95**, 091901 (2009)

Self-assembled bioinspired quantum dots: Optical properties

N. Amdursky, M. Molotskii, E. Gazit, and G. Rosenman

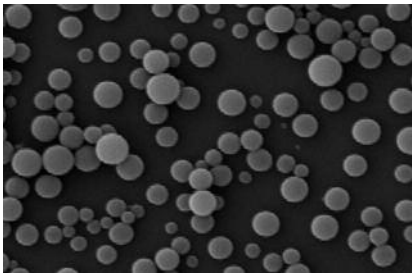

Until now, the wide research field of quantum dots (QDs) focused on inorganic structures. In the present study, the authors report on quantum confinement phenomena found in peptide nanocrystalline regions formed within self-assembly peptide nanospheres. These bioinspired nanostructures exhibit the optical absorption characteristics of QDs with pronounced luminescence of excitons whose origin is at the UV region. Theoretical estimations based on experimental data show that the radius of the self assembled peptide QDs is 1.3 nm.

Appl. Phys. Lett. **94**, 261907 (2009)

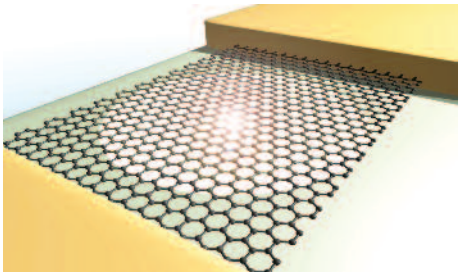

Tuning laser-induced band gaps in graphene

Hernán L. Calvo, Horacio M. Pastawski, Stephan Roche, and Luis E. F. Foa Torres

Could a laser field lead to the much sought-after tunable band gaps in graphene? By using Floquet theory combined with Green's functions techniques, the authors predict that a laser field in the mid-infrared range can produce observable band gaps in the electronic structure of graphene. Furthermore, the authors show how they can be tuned by using the laser polarization. Their results could serve as a guidance to design optoelectronic nanodevices.

Appl. Phys. Lett. **98**, 232103 (2011)

SEMICONDUCTORS

Observation of the integer quantum Hall effect in high quality, uniform wafer-scale epitaxial graphene films

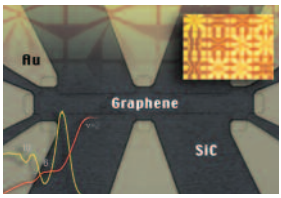

Wei Pan, Stephen W. Howell, Anthony Joseph Ross, III, Taisuke Ohta, and Thomas A. Friedmann

The authors report the observation of the integer quantum Hall states at Landau level fillings of $\nu = 2$, 6, and 10 in a Hall bar device made of a single-layer epitaxial graphene film on the silicon-face of silicon-carbide prepared via argon-assisted graphitization. The two-dimensional electron gas exhibits a low-temperature (at 4 K) carrier mobility of $\sim 14\,000$ cm^2/Vs at the electron density of 6.1×10^{11} cm^{-2}. Furthermore, the sheet resistance obtained from four-probe measurements across the whole area (12×6 mm^2) of another specimen grown under similar condition displays roughly uniform values ($\sim$1600 Ω/square), suggesting that the macroscopic steps and accompanying multilayer graphene domains play a minor role in the low-temperature electronic transport.

Appl. Phys. Lett. **97**, 252101 (2010)

MAGNETICS AND SPINTRONICS

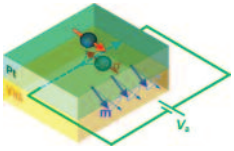

Electric control of magnetization relaxation in thin film magnetic insulators

Zihui Wang, Yiyan Sun, Young-Yeal Song, Mingzhong Wu, Helmut Schultheiß, John E. Pearson, and Axel Hoffmann

Control of magnetization relaxation in magnetic insulators via interfacial spin scattering is demonstrated. The experiments use nanometer-thick yttrium iron garnet (YIG)/Pt layered structures, with the Pt layer biased by an electric voltage. The bias voltage produces a spin current across the Pt thickness. As this current scatters off the YIG surface, it exerts a torque on the YIG surface spins. This torque can reduce or enhance the damping and thereby decrease or increase the ferromagnetic resonance linewidth of the YIG film, depending on the field/current configuration.

Appl. Phys. Lett. **99**, 162511 (2011)

Room-temperature spin-dependent tunneling through molecules

S. Wang, F. J. Yue, J. Shi, Y. J. Shi, A. Hu, Y. W. Du, and D. Wu

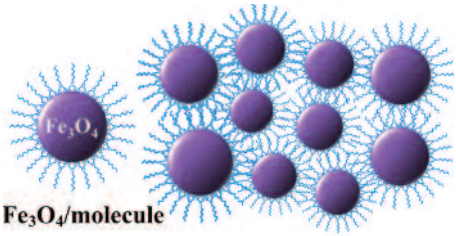

The authors fabricated assemblies of molecular junctions comprised of superparamagnetic Fe_3O_4 nanoparticles self-assembled with alkane molecules of different lengths as the spacer. The electrical resistance increases exponentially over nearly two decades as the molecular length varies from 0.7 to 2.5 nm, indicating that electrons tunnel through the molecules that are chemically bonded with Fe_3O_4 nanoparticles. Up to ~ 21% room-temperature magnetoresistance is observed. Remarkably, the tunneling magnetoresistance ratio stays nearly independent of molecular length, which entails room-temperature spin-conserving transport in organic molecules.

Appl. Phys. Lett. **98**, 172501 (2011)

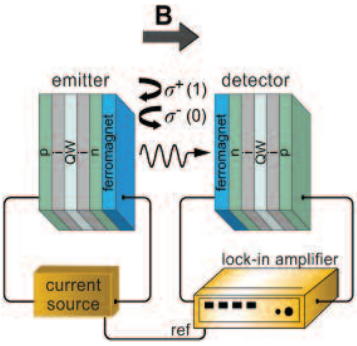

Optical communication of spin information between light emitting diodes

R. Farshchi, M. Ramsteiner, J. Herfort, A. Tahraoui, and H. T. Grahn

For the full implementation of spintronic circuits, it is necessary to transmit spin information from one device to another. Electrons in semiconductors often suffer from high spin relaxation rates, making electrical transport of spin information highly inefficient. In the paper, the authors propose optical transport of spin information as an alternative. They demonstrate that the spin information associated with electrons injected from Co_2FeSi and Fe layers into the quantum wells of spin light emitting diodes (spin-LEDs) can be transported optically in the form of circularly polarized light and deciphered electrically via the magnetic field dependence of the photocurrent in a distant detector spin-LED.

Appl. Phys. Lett. **98**, 162508 (2011)

MAGNETICS AND SPINTRONICS

Ultrafast switching in magnetic tunnel junction based orthogonal spin transfer devices

H. Liu, D. Bedau, D. Backes, J. A. Katine, J. Langer, and A. D. Kent

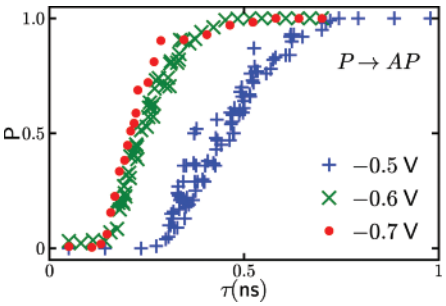

Orthogonal spin-transfer magnetic random access memory (OST-MRAM) uses a spin-polarizing layer magnetized perpendicularly to a free layer to achieve large spin-transfer torques and ultrafast energy efficient switching. The authors have fabricated and studied OST-MRAM devices that incorporate a perpendicularly magnetized spin-polarizing layer and a magnetic tunnel junction, which consists of an in-plane magnetized free layer and synthetic antiferromagnetic reference layer. Reliable switching is observed at room temperature with 0.7 V amplitude pulses of 500 ps duration. The switching is bipolar, occurring for positive and negative polarity pulses, consistent with a precessional reversal mechanism, and requires an energy of less than 450 fJ.

Appl. Phys. Lett. **97**, 242510 (2010)

DIELECTRICS, FERROELECTRICS, AND MULTIFERROICS

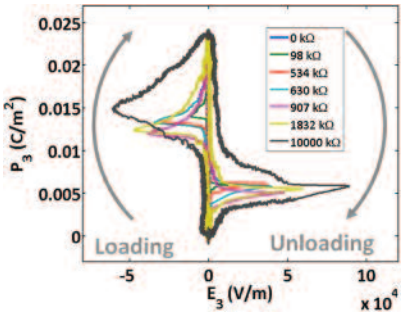

Giant electro-mechanical energy conversion in [011] cut ferroelectric single crystals

Wen D. Dong, Peter Finkel, Ahmed Amin, and Christopher S. Lynch

Giant electro-mechanical energy conversion is demonstrated under a ferroelectric/ferroelectric phase transformation in [011] cut and poled lead titanate-based relaxor perovskite morphotropic single crystals. It is found that under mechanical pre-stress, a relatively small oscillatory stress drives the material reversibly between rhombohedral and orthorhombic phases with a remarkably high polarization and strain jump induced at zero bias electric field and room temperature. The measured electrical output per cycle is more than an order of magnitude larger than that reported for linear piezoelectric materials. Ideal thermodynamic cycles are presented for this electro-mechanical energy conversion followed by a presentation and discussion of the experimental data.

Appl. Phys. Lett. **100**, 042903 (2012)

Powering pacemakers from heartbeat vibrations using linear and nonlinear energy harvesters

M. Amin Karami and Daniel J. Inman

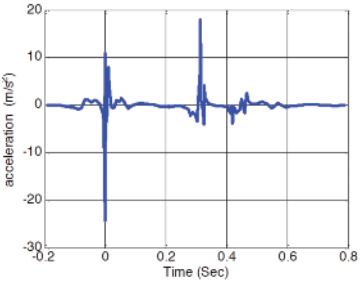

Linear and nonlinear piezoelectric devices are introduced to continuously recharge the batteries of the pacemakers by converting the vibrations from the heartbeats to electrical energy. The power requirement of a pacemaker is very low. However, after few years, patients require another surgical operation just to replace their pacemaker battery. Linear low frequency and nonlinear mono-stable and bi-stable energy harvesters are designed according to the especial signature of heart vibrations. The proposed energy harvesters are robust to variation of heart rate and can meet the power requirement of pacemakers.

Appl. Phys. Lett. **100**, 042901 (2012) | Read the press release

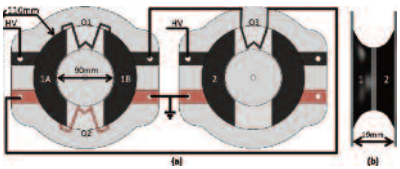

Soft generators using dielectric elastomers

Thomas G. McKay, Benjamin M. O'Brien, Emilio P. Calius, and Iain A. Anderson

The potential to produce light-weight, low-cost, wearable dielectric elastomer generators has been limited by the requirement for bulky rigid, and expensive external circuitry. The authors present a soft dielectric elastomer generator whose stretchable circuit elements are integrated within the membrane. The soft generator achieved an energy density of 10 mJ/g at an efficiency of 12% and simply consisted of low-cost acrylic membranes and carbon grease mounted in a frame.

Appl. Phys. Lett. **98**, 142903 (2011)

Near-room temperature relaxor multiferroic

Dilsom A. Sanchez, A. Kumar, N. Ortega, R. S. Katiyar, and J. F. Scott

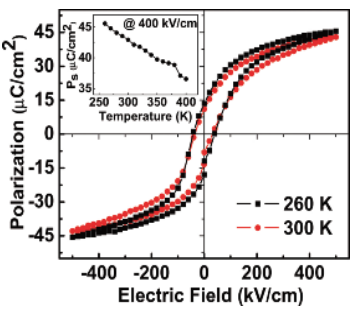

The authors report the fabrication and characterization of highly oriented $Pb(Zr_{0.53}Ti_{0.47})_{0.60}(Fe_{0.5}Ta_{0.5})_{0.40}O_3$ thin films. Dielectric spectra showed a maximum (T_m) around 350 K for 1 kHz that shifted to higher temperatures (by ~ 30 K) with an increase in frequency up to 1 MHz. High dielectric dispersion below and above T_m, low dielectric loss (2%–5%), high dielectric constant (~1380@1 kHz), ferroelectric polarization, and weak magnetic moment are observed. Real and imaginary dielectric data were fitted with a nonlinear Vogel–Fulcher equation, implying a relaxor nature. The ac conductivity shows frequency-dependent conductivity, low loss, and frequency-dependent kinks near T_m.

Appl. Phys. Lett. **97**, 202910 (2010)

Split-illumination electron holography

Toshiaki Tanigaki, Yoshikatsu Inada , Shinji Aizawa, Takahiro Suzuki, Hyun Soon Park, Tsuyoshi Matsuda, Akira Taniyama, Daisuke Shindo, Akira Tonomura

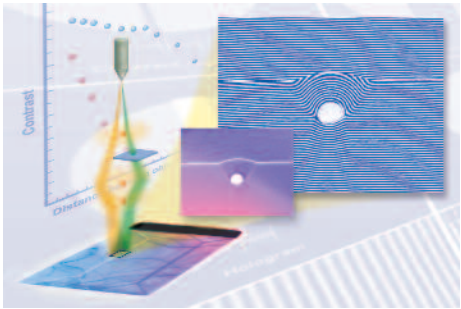

The authors developed a split-illumination electron holography that uses an electron biprism in the illuminating system and two biprisms (applicable to one biprism) in the imaging system, enabling holographic interference micrographs of regions far from the sample edge to be obtained. Using a condenser biprism, they split an electron wave into two coherent electron waves: one wave is to illuminate an observation area far from the sample edge in the sample plane and the other wave to pass through a vacuum space outside the sample. The split-illumination holography has the potential to greatly expand the breadth of applications of electron holography.

Appl. Phys. Lett. **101**, 043101 (2012)

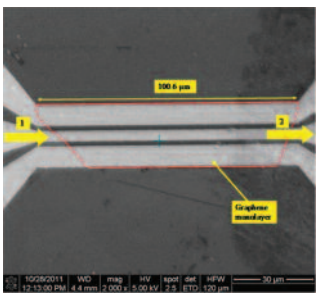

Graphene radio: Detecting radiowaves with a single atom sheet

M. Dragoman, D. Neculoiu, A. Cismaru, G. Deligeorgis, G. Konstantinidis, and D. Dragoman

The authors present the experimental evidence of RF demodulation by a graphene monolayer embedded in a coplanar structure. The demodulator was tested in the frequency range from 100 MHz to 25 GHz using amplitude modulated input signals. An input power of 0 dBm (1 mW) was used, which is the typical power emitted for short-range wireless communication systems, such as Bluetooth. The graphene demodulator exhibits good signal responsivity in the frequency range associated to industrial, scientific and medical radio band with a peak of 1100 V/W at 3.5 GHz.

Appl. Phys. Lett. **101**, 033109 (2012)

Carbon nanotube based ultra-low voltage integrated circuits: Scaling down to 0.4 V

Li Ding, Shibo Liang, Tian Pei, Zhiyong Zhang, Sheng Wang, Weiwei Zhou, Jie Liu, and Lian-Mao Peng

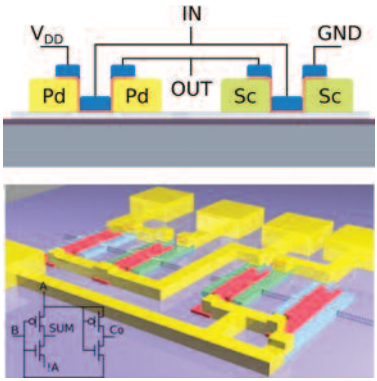

Carbon nanotube (CNT) based integrated circuits (ICs) including basic logic and arithmetic circuits were demonstrated working under a supply voltage low as 0.4 V, which is much lower than that used in conventional silicon ICs. The low limit of supply voltage of the CNT circuits is determined by the degraded noise margin originated from the process inducing threshold voltage fluctuation. The power dissipation of CNT ICs can be remarkably reduced by scaling down the supply voltage, and it is of crucial importance for the further developments of nanoelectronics ICs with higher integration density.

Appl. Phys. Lett. **100**, 263116 (2012)

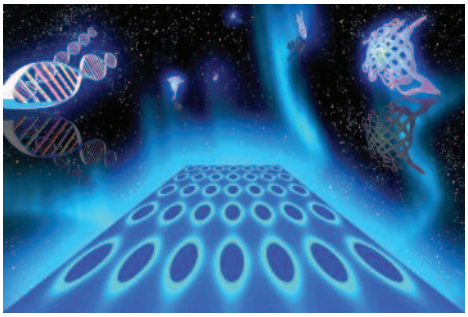

Silicon-based reproducible and active surface-enhanced Raman scattering substrates for sensitive, specific, and multiplex DNA detection

Z. Y. Jiang, X. X. Jiang, S. Su, X. P. Wei, S. T. Lee, and Y. He

Silicon-based active and reproducible surface-enhanced Raman scattering (SERS) substrate, i.e., silver nanoparticles decorated-silicon wafers (AgNPs@Si), is employed for constructing high-performance sensors. Significantly, the AgNPs@Si, facilely prepared via *in situ* AgNPs growth on silicon wafers, features excellent SERS reproducibility and high enhancement factor. This experiment further demonstrates such resultant silicon-based SERS substrate is efficacious for multiplex, sensitive, and specific DNA detection. In particular, single-base mismatched DNA with low concentrations is readily discriminated by using the AgNPs@Si. Moreover, the silicon-based sensor exhibits adequate multiplexing capacity, enabling unambiguous identification of the dual-target DNA detection.

Appl. Phys. Lett. **100**, 203104 (2012)

A graphene electron lens

L. Gerhard, E. Moyen, T. Balashov, I. Ozerov, M. Portail, H. Sahaf, L. Masson, W. Wulfhekel, and M. Hanbücken

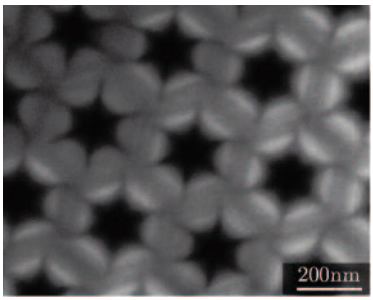

An epitaxial layer of graphene was grown on a pre patterned 6H-SiC(0001) crystal. The graphene smoothly covers the hexagonal nano-holes in the substrate without the introduction of small angle grain boundaries or dislocations. This is achieved by an elastic deformation of the graphene by ≈0.3% in accordance to its large elastic strain limit. This elastic stretching of the graphene leads to a modification of the band structure and to a local lowering of the electron group velocity of the graphene. They propose to use this effect to focus two-dimensional electrons in analogy to simple optical lenses.

Appl. Phys. Lett. **100**, 153106 (2012)

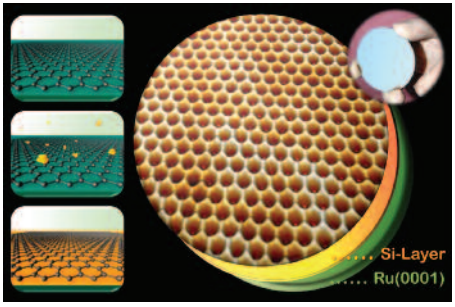

Silicon layer intercalation of centimeter-scale, epitaxially grown monolayer graphene on Ru(0001)

Jinhai Mao, Li Huang, Yi Pan, Min Gao, Junfeng He, Haitao Zhou, Haiming Guo, Yuan Tian, Qiang Zou, Lizhi Zhang, Haigang Zhang, Yeliang Wang, Shixuan Du, Xingjiang Zhou, A. H. Castro Neto, and Hong-Jun Gao

The authors develop a strategy for graphene growth on Ru(0001) followed by silicon-layer intercalation that not only weakens the interaction of graphene with the metal substrate but also retains its superlative properties. This G/Si/Ru architecture, produced by silicon-layer intercalation approach (SIA), was characterized by scanning tunneling microscopy/spectroscopy and angle resolved electron photoemission spectroscopy. These experiments show high structural and electronic qualities of this new composite. The SIA allows for an atomic control of the distance between the graphene and the metal substrate that can be used as a top gate. These results show potential for the next generation of graphene-based materials with tailored properties.

Appl. Phys. Lett. **100**, 093101 (2012)

Nanofluid based optical sensor for rapid visual inspection of defects in ferromagnetic materials

V. Mahendran and John Philip

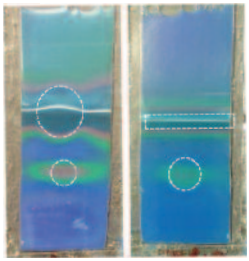

The authors have developed a simple sensor for imaging internal defects in materials using a magnetically polarizable nanoemulsion. The gradient in the magnetic flux lines around the defective region leads to the formation of one-dimensional nanodroplet arrays along the field direction, which incredibly diffract the incident white light to produce bright colors. As the diffracted wavelength has a direct correlation with the defect features, this approach enable visual inspection of ferromagnetic components and has several advantages over existing flux leakage sensors in terms of cost, re-usability and complexity.

Appl. Phys. Lett. **100**, 073104 (2012)

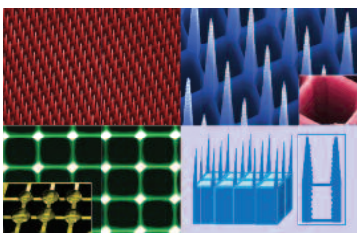

Multifunctional silicon inspired by a wing of male *Papilio ulysse*

Sang H. Yun, Hyung-Seok Lee, Young Ha Kwon, Mats Göthelid, Sang Mo Koo, Lars Wågberg, Ulf O. Karlsson, and Jan Linnros

Effective entrapment of air and light is a key element for maintaining stable superhydrophobicity and enhancing anti-reflection or absorption. Inspired by a wing of male *Papilio ulysse* having a unique structure for enabling effective trapping of air and light, the authors demonstrate that the structure consisting of well-defined multilayer decorated by nanostructures can be obtained on a silicon wafer by a simple microelectromechanical process, consequently resulted in stable superhydrophobocity under static and dynamic conditions, and strong wideband optical absorption.

Appl. Phys. Lett. **100**, 033109 (2012)

Ultra-thin plasmonic optical vortex plate based on phase discontinuities

Patrice Genevet, Nanfang Yu, Francesco Aieta, Jiao Lin, Mikhail A. Kats, Romain Blanchard, Marlan O. Scully, Zeno Gaburro, and Federico Capasso

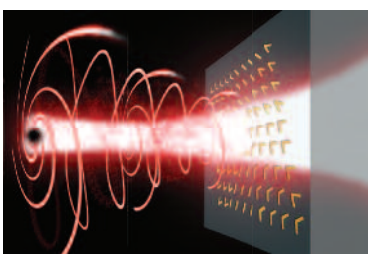

A flat optical device that generates optical vortices with a variety of topological charges is demonstrated. This device spatially modulates light beams over a distance much smaller than the wavelength in the direction of propagation by means of an array of V-shaped plasmonic antennas with sub-wavelength separation. Optical vortices are shown to develop after a sub-wavelength propagation distance from the array, a feature that has major potential implications for integrated optics.

Appl. Phys. Lett. **100**, 013101 (2012)

Sensory and short-term memory formations observed in a Ag_2S gap-type atomic switch

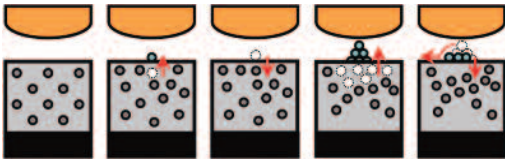

Takeo Ohno, Tsuyoshi Hasegawa, Alpana Nayak, Tohru Tsuruoka, James K. Gimzewski, and Masakazu Aono

Memorization caused by the change in conductance in a Ag_2S gap-type atomic switch was investigated as a function of the amplitude and width of input voltage pulses (V_{in}). The conductance changed little for the first few V_{in}, but the information of the input was stored as a redistribution of Ag-ions in the Ag_2S, indicating the formation of sensory memory. After a certain number of V_{in}, the conductance increased abruptly followed by a gradual decrease, indicating the formation of short-term memory (STM). The authors found that the probability of STM formation depends strongly on the amplitude and width of V_{in}, which resembles the learning behavior of the human brain.

Appl. Phys. Lett. **99**, 203108 (2011)

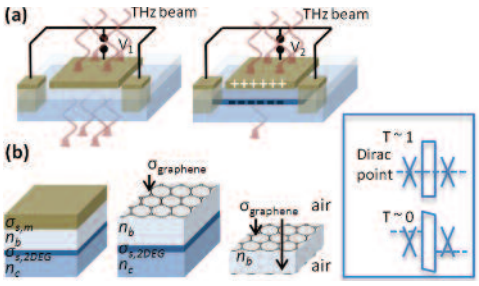

Unique prospects for graphene-based terahertz modulators

Berardi Sensale-Rodriguez, Tian Fang, Rusen Yan, Michelle M. Kelly, Debdeep Jena, Lei Liu, and Huili (Grace) Xing

The modulation depth of two-dimensional electron-gas (2DEG) based terahertz (THz) modulators using AlGaAs/GaAs hetero-structures with metal gates is inherently limited to <30%. The metal gate not only attenuates the THz signal but also severely degrades modulation depth. Metal losses can be significantly reduced employing an alternative material with tunable conductivity. Graphene presents a unique solution to this problem due to its symmetric band structure and extraordinarily high hole mobility. In this work, the authors show that it is possible to achieve a modulation depth of >90% while simultaneously minimizing signal attenuation to <5% by tuning the Fermi level at its Dirac point.

Appl. Phys. Lett. **99**, 113104 (2011)

Barrier-free tunneling in a carbon heterojunction transistor

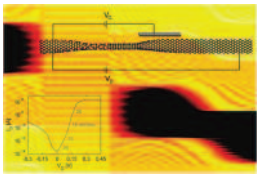

Youngki Yoon and Sayeef Salahuddin

Recently, it has been experimentally shown that a graphene nanoribbon (GNR) can be obtained by unzipping a carbon nanotube (CNT). This makes it possible to fabricate all-carbon heterostructures that have a unique interface between a CNT and a GNR. The authors demonstrate that such a heterojunction may be utilized to obtain a unique transistor operation. By performing a self-consistent nonequilibrium Green's function based calculation on an atomistically defined structure, they show that such a transistor may reduce energy dissipation below the classical limit while not compromising speed—thus providing an alternate route toward ultralow-power, high-performance carbon-heterostructure electronics.

Appl. Phys. Lett. **97**, 033102 (2010)

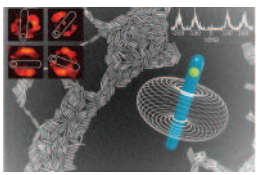

Room temperature-dipolelike single photon source with a colloidal dot-in-rod

Ferruccio Pisanello, Luigi Martiradonna, Godefroy Leménager, Piernicola Spinicelli, Angela Fiore, Liberato Manna, Jean-Pierre Hermier, Roberto Cingolani, Elisabeth Giacobino, Massimo De Vittorio, and Alberto Bramati

The authors propose colloidal CdSe/CdS dots in rods as nonclassical sources for quantum information technology. Such nanoemitters show specific properties such as strongly polarized emission of on-demand single photons at room temperature, dipolelike behavior and mono-exponential recombination rates, making us envision their suitability as sources of single photons with well defined quantum states in quantum cryptography based devices.

Appl. Phys. Lett. **96**, 033101 (2010)

ORGANIC ELECTRONICS AND PHOTONICS

Photoinduced write-once read-many-times memory device based on DNA biopolymer nanocomposite

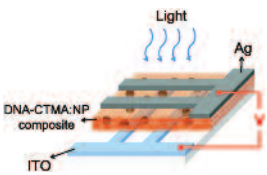

Yu-Chueh Hung, Wei-Ting Hsu, Ting-Yu Lin, and Ljiljana Fruk

The authors demonstrate a photoinduced write-once read-many-times (WORM) organic memory device based on DNA biopolymer nanocomposite. The device consists of a single biopolymer layer sandwiched between electrodes, in which electrical bistability is activated by *in situ* formation of silver nanoparticles embedded in biopolymer upon light irradiation. The device exhibits a switching effect to high conductivity above a threshold of 2.6 V and a good retention property. This facile technique, taking advantage of DNA's affinity for metals and solution processing, can optically manipulate the properties of DNA nanocomposite thin films, which holds promise for optical storage and plasmonic applications.

Appl. Phys. Lett. **99**, 253301 (2011)

Transparent, near-infrared organic photovoltaic solar cells for window and energy-scavenging applications

Richard R. Lunt and Vladimir Bulovic

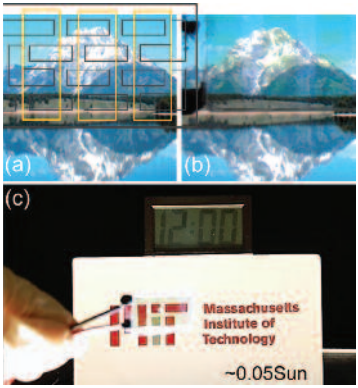

The authors fabricate near-infrared absorbing organic photovoltaics that are highly transparent to visible light. By optimizing near-infrared optical-interference, they demonstrate power efficiencies of 1.3±0.1% with simultaneous average visible transmission of >65%. Subsequent incorporation of near-infrared distributed-Bragg-reflector mirrors leads to an increase in the efficiency to 1.7±0.1%, approaching the 2.4±0.2% efficiency of the opaque cell, while maintaining high visible-transparency of >55%. Finally, they demonstrate that a series-integrated array of these transparent cells is capable of powering electronic devices under near-ambient lighting. This architecture suggests strategies for high-efficiency power-generating windows and highlights an application uniquely benefiting from excitonic electronics.

Appl. Phys. Lett. **98**, 113305 (2011)

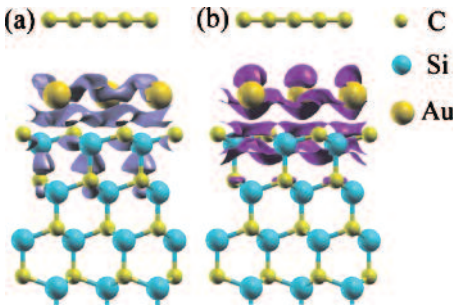

A route to strong *p*-doping of epitaxial graphene on SiC

Y. C. Cheng and U. Schwingenschlögl

The effects of Au intercalation on the electronic properties of epitaxial graphene grown on SiC{0001} substrates are studied using first principles calculations. A graphene monolayer on SiC{0001} restores the shape of the pristine graphene dispersion, where doping levels between strongly *n*-doped and weakly *p*-doped can be achieved by altering the Au coverage. The authors predict that Au intercalation between the two C layers of bilayer graphene grown on SiC{0001} makes it possible to achieve a strongly *p*-doped graphene state, where the *p*-doping level can be controlled by means of the Au coverage.

Appl. Phys. Lett. **97**, 193304 (2010)

High-power and high-speed organic three-dimensional transistors with submicrometer channels

M. Uno, Y. Hirose, T. Uemura, K. Takimiya, Y. Nakazawa, and J. Takeya

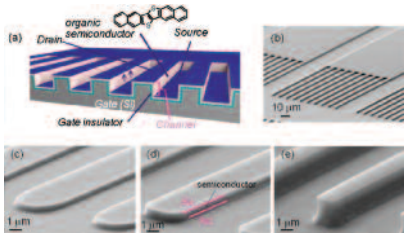

Three-dimensional organic field-effect transistors with high current density and high switching speed are developed with multiple submicrometer channels arranged perpendicularly to substrates. The short channel length is defined by the height of a multicolumnar structure without an electron-beam-lithography process. For devices using dinaphtho[2,3-b:2′,3′-f]thieno[3,2-b]thiophene, extremely high current density exceeding 10 A/cm^2 and fast switching within 0.2 μs are realized with an on-off ratio of 10^5. The unprecedented performance is beyond general requirements to control organic light-emitting diodes, so that even more extensive applications to higher-speed active-matrices and display-driving circuits can be realized with organic semiconductors.

Appl. Phys. Lett. **97**, 013301 (2010)

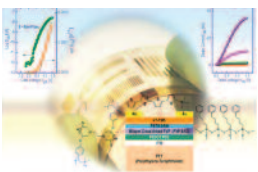

Solution-processed flexible organic transistors showing very-low subthreshold slope with a bilayer polymeric dielectric on plastic

Zihong Liu, Joon Hak Oh, Mark E. Roberts, Peng Wei, Bipul C. Paul, Masaki Okajima, Yoshio Nishi, and Zhenan Bao

The authors demonstrate low-voltage, solution-processed organic transistors on rough plastic substrates with a carrier mobility over 0.2 cm^2/Vs, a turn-on voltage of near 0 V, and a *record* low subthreshold slope of ~ 80 mV/decade in ambient conditions. These exceptional characteristics are attributed to (1) a device stacking architecture with a conducting polymeric gate and a double layered dielectric composed of low-temperature cross-linked poly(4-vinylphenol), (2) a low interface trap density achieved by modifying the dielectric surface with a phenyl-terminated self-assembled monolayer from 4-phenylbutyltrichlorosilane, and (3) controlled crystallization of a small-molecule organic semiconductor film with favorable charge transport microstructure and a low bulk trap density as deposited by an optimized solution-shearing process. The device performance under different operating voltages was also examined and discussed.

Appl. Phys. Lett. **94**, 203301 (2009)

Vacuum nanoelectronics: Back to the future?—Gate insulated nanoscale vacuum channel transistor

Jin-Woo Han, Jae Sub Oh, and M. Meyyappan

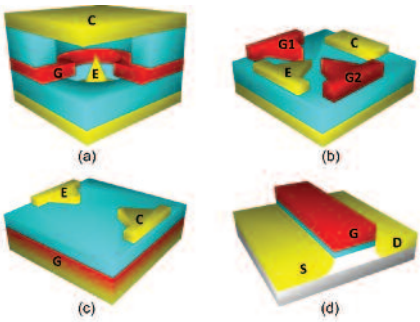

A gate-insulated vacuum channel transistor was fabricated using standard silicon semiconductor processing. Advantages of the vacuum tube and transistor are combined here by nanofabrication. A photoresist ashing technique enabled the nanogap separation of the emitter and the collector, thus allowing operation at less than 10 V. A cut-off frequency f_T of 0.46 THz has been obtained. The nanoscale vacuum tubes can provide high frequency/power output while satisfying the metrics of lightness, cost, lifetime, and stability at harsh conditions, and the operation voltage can be decreased comparable to the modern semiconductor devices.

Appl. Phys. Lett. **100**, 213505 (2012)

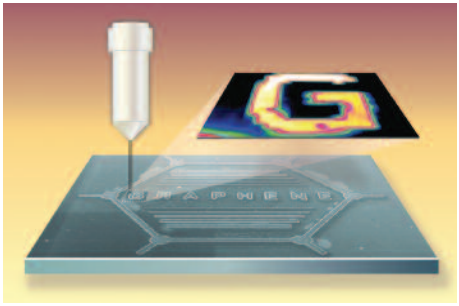

Drawing graphene nanoribbons on SiC by ion implantation

S. Tongay, M. Lemaitre, J. Fridmann, A. F. Hebard, B. P. Gila, and B. R. Appleton

The authors describe a straightforward technique for selective graphene growth and nanoribbon production onto 4H- and 6H-SiC. The technique presented is as easy as ion implanting regions where graphene layers are desired followed by annealing to 100 °C below the graphitization temperature (T_G) of SiC. They find that ion implantation of SiC lowers the T_G, allowing selective graphene growth at temperatures below the T_G of pristine SiC and above T_G of implanted SiC. This results in an approach for patterning device structures ranging from a couple tens of nanometers to microns in size without using conventional lithography and chemical processing.

Appl. Phys. Lett. **100**, 073501 (2012)

DEVICE PHYSICS

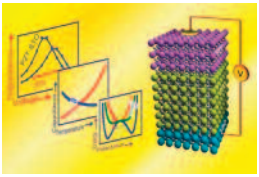

Experimental evidence of ferroelectric negative capacitance in nanoscale heterostructures

Asif Islam Khan, Debanjan Bhowmik, Pu Yu, Sung Joo Kim, Xiaoqing Pan, Ramamoorthy Ramesh, and Sayeef Salahuddin

The authors report a proof-of-concept demonstration of negative capacitance effect in a nanoscale ferroelectric-dielectric heterostructure. In a bilayer of ferroelectric $Pb(Zr_{0.2}Ti_{0.8})O_3$ and dielectric $SrTiO_3$, the composite capacitance was observed to be larger than the constituent $SrTiO_3$ capacitance, indicating an effective negative capacitance of the constituent $Pb(Zr_{0.2}Ti_{0.8})O_3$ layer. Temperature is shown to be an effective tuning parameter for the ferroelectric negative capacitance and the degree of capacitance enhancement in the heterostructure. Landau's mean field theory based calculations show qualitative agreement with observed effects. This work underpins the possibility that by replacing gate oxides by ferroelectrics in nanoscale transistors, the sub threshold slope can be lowered below the classical limit (60 mV/decade).

Appl. Phys. Lett. **99**, 113501 (2011)

BIOPHYSICS AND BIO-INSPIRED SYSTEMS

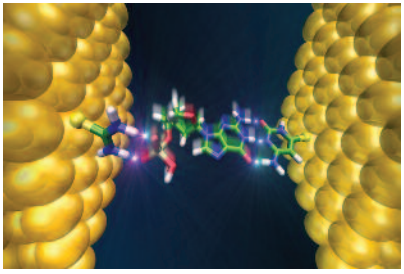

Double-functionalized nanopore-embedded gold electrodes for rapid DNA sequencing

Biswarup Pathak, Henrik Löfås, Jariyanee Prasongkit, Anton Grigoriev, Rajeev Ahuja, and Ralph H. Scheicher

The authors have studied the effect of double-functionalization on gold electrodes for improving nanopore-based DNA sequencing. The functionalizing molecular probes are, respectively, capable of temporarily forming hydrogen bonds with both the nucleobase part and the phosphate group of the target DNA, thus potentially minimizing the structural fluctuations of a single-stranded DNA molecule passing between the gold electrodes. The results of our first-principles study indicate that the proposed setup yields current signals that differ by at least 1 order of magnitude for the four different nucleic acid bases, thus offering the possibility to electrically distinguish them.

Appl. Phys. Lett. **100**, 023701 (2012)

BIOPHYSICS AND BIO-INSPIRED SYSTEMS

Physics of ultra-high bioproductivity in algal photobioreactors

Efrat Greenwald, Jeffrey M. Gordon, and Yair Zarmi

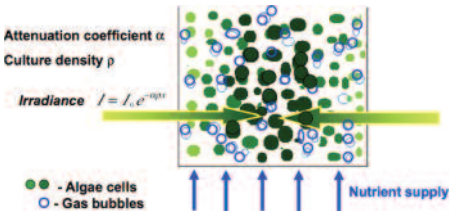

Cultivating algae at high densities in thin photobioreactors engenders time scales for random cell motion that approach photosynthetic rate-limiting time scales. This synchronization allows bioproductivity above that achieved with conventional strategies. The authors show that a diffusion model for cell motion (1) accounts for high bioproductivity at irradiance values previously deemed restricted by photoinhibition, (2) predicts the existence of optimal culture densities and their dependence on irradiance, consistent with available data, (3) accounts for the observed degree to which mixing improves bioproductivity, and (4) provides an estimate of effective cell diffusion coefficients, in accord with independent hydrodynamic estimates.

Appl. Phys. Lett. **100**, 143703 (2012)

INTERDISCIPLINARY AND GENERAL PHYSICS

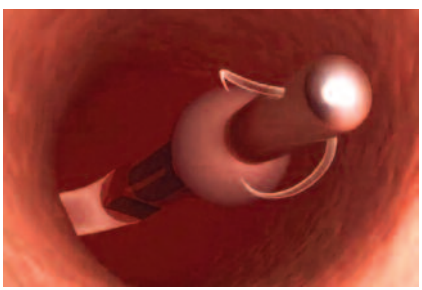

Multi-degree-of-freedom ultrasonic micromotor for guidewire and catheter navigation: The NeuroGlide actuator

Cheol-Ho Yun, Leslie Y. Yeo, James R. Friend, and Bernard Yan

A 240-μm diameter ultrasonic micromotor is presented as a potential solution for an especially difficult task in minimally invasive neurosurgery, navigating a guidewire to an injury in the neurovasculature as the first step of surgery. The peak no-load angular velocity and maximum torque were 600 rad/s and 1.6 nN-m, respectively, and the authors obtained rotation about all three axes. By using a burst drive scheme, open-loop position and speed control were achieved. The construction method and control scheme proposed in this study remove most of the current limitations in minimally invasive, catheter-based actuation, enabling minimally invasive vascular surgery concepts to be pursued for a broad variety of applications.

Appl. Phys. Lett. **100**, 164101 (2012)

Flexible solid-state paper based carbon nanotube supercapacitor

Shan Hu, Rajesh Rajamani, and Xun Yu

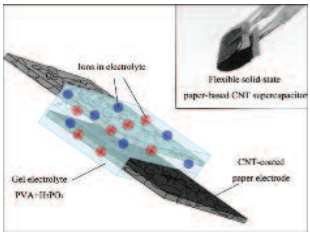

This paper presents a flexible solid-state supercapacitor of high energy density. The electrodes of the supercapacitor are made of porous and absorbent cotton paper coated with single-wall carbon nanotubes. To ensure all solid-state configuration, a solid-state polymer-based electrolyte (poly (vinyl alcohol)/phosphoric acid) is used. The as-fabricated supercapacitor can be charged to over 3 V. It has high specific capacitance and high energy density of 115.8301 F/g carbon and 48.8587 Wh/kg carbon. Its performance is comparable to that of commercial supercapacitors, which need to utilize liquid electrolytes. Flexible solid-state supercapacitors offer several significant advantages for use in hybrid electric vehicles.

Appl. Phys. Lett. **100**, 104103 (2012)

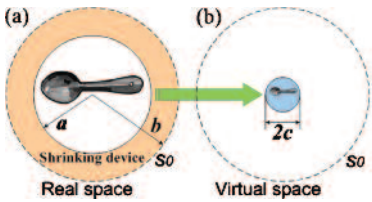

Shrinking an arbitrary object as one desires using metamaterials

Wei Xiang Jiang, Tie Jun Cui, Xin Mi Yang, Hui Feng Ma, and Qiang Cheng

Based on transformation optics, the authors present a shrinking device, which can transform an arbitrary object virtually into a small-size object with different material parameters as one desires. Such an illusion device will confuse the detectors or the viewers, and hence the real size and material parameters of the enclosed object cannot be perceived. They fabricated and measured a shrinking device by using metamaterials, which works at the nonresonant frequency and has low loss. The device has been validated by both numerical simulations and experiments on circular and square objects. Good shrinking performance has been demonstrated.

Appl. Phys. Lett. **98**, 204101 (2011)

Frost formation and ice adhesion on superhydrophobic surfaces

Kripa K. Varanasi, Tao Deng, J. David Smith, Ming Hsu, and Nitin Bhate

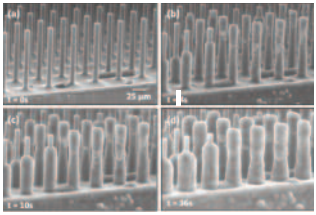

The authors study frost formation and its impact on icephobic properties of superhydrophobic surfaces. Using an environmental scanning electron microscope, they show that frost nucleation occurs indiscriminately on superhydrophobic textures without any particular spatial preference. Ice adhesion measurements on superhydrophobic surfaces susceptible to frost formation show increased adhesion over smooth surfaces with a strong linear trend with the total surface area. These studies indicate that frost formation significantly compromises the icephobic properties of superhydrophobic surfaces and poses serious limitations to the use of superhydrophobic surfaces as icephobic surface treatments for both on-ground and in-flight applications.

Appl. Phys. Lett. **97**, 234102 (2010)

APL 50th ANNIVERSARY EDITOR'S PICKS

In this collection, the Editor has selected a few of the many notable APL articles published from 2009 through 2012 that present ground-breaking research. This collection illustrates only a small fraction of the critical research published in APL over the past fifty years but is representative of the broad cross section of topics that the Journal covers. The articles listed in the collection are freely available online at apl.aip.org until the end of September 2013.

APL Editorial Office
NGHI Q. LAM
Editor, *Applied Physics Letters*
Argonne National Laboratory
Building 203, Room R-127
9700 South Cass Avenue
Argonne, IL 60439-4843, USA

Telephone: 630-252-4200
Fax: 630-252-4973
E-mail: apl@anl.gov
Submissions: apl.peerx-press.org

AIP Publishing
American Institute of Physics
Suite 1NO1
2 Huntington Quadrangle
Melville, NY 11747-4502, USA
E-mail: jrnlpub@aip.org

apl.aip.org/50th_anniversary_editors_picks

Scan this QR code with your smartphone or tablet to visit our website

apl.aip.org